Compressive Passive Millimeter Wave Imaging with Extended Depth of Field

Vishal M. Patel

Center for Automation Research, UMIACS
University of Maryland
College Park, Maryland 20742
USA

pvishalm@umiacs.umd.edu

Joseph N. Mait, FELLOW SPIE

U.S. Army Research Laboratory
RDRL-SER
2800 Powder Mill Road
Adelphi, Maryland 20783
USA

joseph.mait@us.army.mil

Abstract. In this paper, we introduce a millimeter wave imaging modality with extended depth-of-field that provides diffraction limited images with reduced spatial sampling. The technique uses a cubic phase element in the pupil of the system and a nonlinear recovery algorithm to produce images that are insensitive to object distance. We present experimental results that validate system performance and demonstrate a greater than four-fold increase in depth-of-field with a reduction in sampling requirements by a factor of at least two. *DOI: 10.0000/XXXX*

Subject terms: Computational imaging, millimeter wave imaging, extended depth-of-field, image reconstruction, sparsity.

Manuscript compiled April 11, 2012

1 Introduction

Interest in millimeter wave (mmW) and terahertz imaging has increased in the past several years.[1–3] This interest is driven, in part, by the ability of these frequencies to penetrate poor weather and other obscurants, such as clothes and polymers. Millimeter waves are electromagnetic waves typically defined in the 30 to 300 GHz range with corresponding wavelengths between 10 to 1 mm. Radiation at these these frequencies is non-ionizing and is therefore considered safe for human use. Applications of this technology include the detection of concealed weapons, explosives and contraband.[1]

However, when used for short range imaging (as opposed to infinite conjugate imaging in astronomy) most mmW systems have a narrow depth-of-field (DoF), the distance over which an object is considered in focus. If individuals are moving toward an imager through a corridor, the weapons would be visible only for the brief moment when they were in the depth-of-field. This is one reason individuals are scanned in portals. However, extensions to scanning over a volume could provide scanning without creating bottlenecks, for example, in a public marketplace where security is important but a visible display of security might be counterproductive. In,[3] Mait *et al.* presented a computational imaging method to extend the depth-of-field of a passive mmW imaging system to allow for operation over a volume. The method uses a cubic phase element in the pupil plane of the system in combination with post-detection signal processing to render system operation relatively insensitive to object distance. Using this technique increased the depth-of-field of a 94 GHz imager to 68” (1727 mm), which is four times its conventional value of approximately 17” (432 mm).[3]

Unfortunately this system, as well as others discussed in the literature,[1,2] form an image by scanning a single-beam in azimuth and elevation. Although real-time mmW imaging has also been demonstrated using an array of sensors, such systems introduce complexity and are costly. Although total scan time per sample is a function of positioning and integration times, to first order at least, if one can reduce the number of samples and maintain imaging performance, one can increase scan rates with minimal detriment. To reduce the number of samples required to form an image, researchers have applied compressive sampling methods[4,5] to mmW imaging.[6–11]

In this paper, we describe a passive mmW imaging system with extended depth-of-field that can produce images with reduced number of samples. Our method relies on using a far fewer number of measurements than the conventional systems and can reduce the sampling requirements significantly, especially when scanning over a volume. We show that if the mmW image is assumed sparse in some transform domain, then one can reconstruct a good estimate of the image using this new image formation algorithm.

1.1 *Paper organization*

The organization of the paper is as follows. Section 2 provides background information on passive mmW imaging with extended depth-of-field using a 94GHz system. Section 3 provides background

on compressive sensing. The proposed undersampling scheme is described in Section 4. We demonstrate experimental results in Section 5 and Section 6 concludes the paper with a brief summary and discussion.

2 Millimeter wave imaging system

In[3] we used a 94-GHz Stokes-vector radiometer to form images by raster scanning the system's single beam. The radiometer has a thermal sensitivity of 0.3 K with a 30-ms integration time and 1-GHz bandwidth. A Cassegrain antenna with a 24" (610 mm) diameter primary parabolic reflector and a 1.75" (44.5 mm) diameter secondary hyperbolic reflector is mounted to the front of the radiometer receiver. The position of the hyperbolic secondary is variable but fixed in our system such that the effective focal length is 6" (152.4 mm) (i.e., the system is $f/4$) and the image distance is 5.81" (147.6 mm).

One can model the 94-GHz imaging system as a linear, spatially incoherent, quasi-monochromatic system.[3] The intensity of the detected image can be represented as a convolution between the intensity of the image predicted by the geometrical optics with the system point spread function[12]

$$ii(x,y) \triangleq |i(x,y)|^2 = o_g(x,y) * *h(x,y), \tag{1}$$

where $**$ represents two-dimensional convolution. The function $o_g(x,y)$ represents the inverted, magnified image of the object that a ray-optics analysis of the system predicts.

The second term in Eq. (1), $h(x,y)$, is the incoherent point spread function (PSF) that accounts for wave propagation through the aperture

$$h(x,y) = \frac{1}{(\lambda f)^4}\left|p\left(\frac{-x}{\lambda f}, \frac{-y}{\lambda f}\right)\right|^2, \tag{2}$$

where $p(x/\lambda f, y/\lambda f)$ is the coherent point spread function. The function $p(x,y)$ is the inverse Fourier transform of the system pupil function $P(u,v)$,

$$p(x,y) = FT^{-1}[P(u,v)].$$

Without loss of generality, we assume object and image are $N \times N$ arrays. We can then rewrite Eq. (1) in matrix notation as

$$\mathbf{i} = \mathbf{H}\mathbf{o}_g, \tag{3}$$

where $\mathbf{i}$ and $\mathbf{o}_g$ are $N^2 \times 1$ lexicographically ordered column vectors representing the $N \times N$ arrays $ii(x,y)$ and $o_g(x,y)$, respectively, and $\mathbf{H}$ is the $N^2 \times N^2$ matrix that models the incoherent point spread function $h(x,y)$.

Displacement of an object from the nominal object plane of the imaging system introduces a phase error in the pupil function that increases the width of a point response and produces an out of

focus image. The system's depth-of-field is defined as the distance in object space over which an object can be placed and still produce an in-focus image.

For a 94 GHz imager with an aperture diameter $D = 24$" and object distance $d_o = 180$" (4572 mm), $DoF \approx 17.4$" (442 mm) which ranges from 175.2" (4450.1 mm) to 192.6" (4892 mm).[3]

In,[3] we demonstrated how to extend the DoF using a cubic phase element in conjunction with post-detection processing. The cubic phase element $P_c(u, v)$ is

$$P_c(u, v) = \exp(j\theta_c(u, v))\texttt{rect}\left(\frac{u}{\xi_u}, \frac{v}{\xi_v}\right), \tag{4}$$

where

$$\theta_c(u, v) = (\pi\gamma)\left[\left(\frac{2u}{\xi_u}\right)^3 + \left(\frac{2v}{\xi_v}\right)^3\right]$$

and `rect` is the rectangular function. The phase function is separable in the u and v spatial frequencies and has spatial extent ξ_u and ξ_v along the respective axis. The constant γ represents the strength of the cubic phase. Fig. 1 shows the cubic phase element mounted on the antenna. Although fabrication introduces artifacts from spatial and phase quantization into the cubic element response, their impact on performance is negligible.[3]

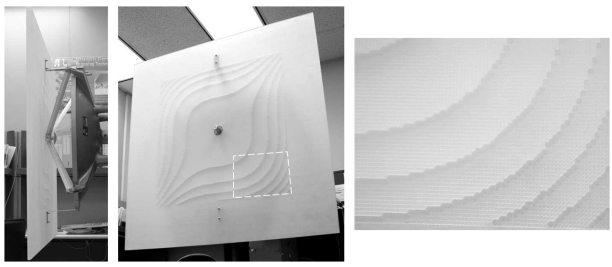

(a) (b) (c)

Fig. 1 Cubic phase element. (a) Side view of the cubic phase element mounted the antenna. (b) Front view. (c) Detail of fabricated cubic phase element.

Fig. 2 shows the measured PSFs for conventional imaging and imaging with a cubic phase. The width of the in-focus PSF at 180" (4572 mm) is approximately 2 mm, which is consistent with a 1 mm pixel width. The out-of-focus planes are at approximately four times and twice the DOF at 113" (2870 mm) and 146.5" (3721 mm), respectively, which correspond to 0.32 and 0.16 wavelengths of defocus. Note that the response of the cubic phase system is relatively unchanged, whereas the response of the conventional system changes considerably. A post-detection signal processing step is necessary to produce a well-defined sharp response.[13–15]

If we assume a linear post-detection process

$$i_p(x, y) = ii(x, y) * *w(x, y), \tag{5}$$

we can implement $w(x,y)$ as a Wiener filter in frequency space,

$$W(u,v) = \frac{H_c^*(u,v)}{|H_c(u,v)|^2 + \frac{K^{-2}\hat{\Phi}_N(u,v)}{\hat{\Phi_L}(u,v)}}, \tag{6}$$

where $H_c(u,v)$ is the optical transfer function associated with the cubic phase element, $W(u,v)$ is the Fourier transform of $w(x,y)$, the parameter K is a measure of the signal-to-noise ratio, and the functions $\hat{\Phi}_L$ and $\hat{\Phi}_N$ are the expected power spectra of the object and noise, respectively. The optical transfer function is usually estimated from the experimentally measured point responses. One can view the estimated $i_p(x,y)$ as a diffraction limited response. We rewrite Eq. (5) in matrix notation as

$$\begin{aligned} \mathbf{i}_p &= \mathbf{W}\mathbf{i} \\ &= \mathbf{W}\mathbf{H}\mathbf{o}_g, \end{aligned} \tag{7}$$

where $\mathbf{i}_p$ is the $N^2 \times 1$ column vector corresponding to array $i_p(x,y)$ and $\mathbf{W}$ is the $N^2 \times N^2$ convolution matrix corresponding to the Wiener filter $w(x,y)$. The issue we address in the remainder is with what fidelity can we estimate $\mathbf{i}_p$ using less than N^2 measurements of $\mathbf{i}$.

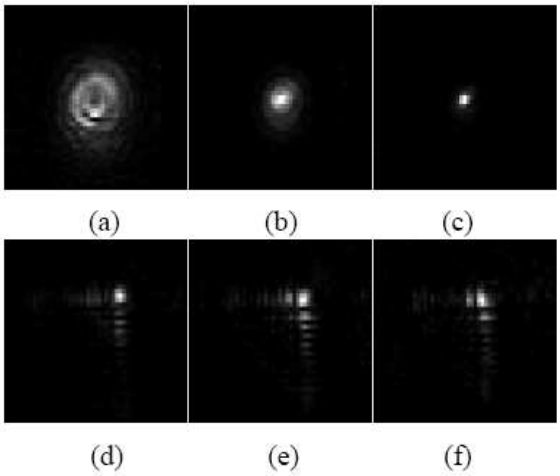

Fig. 2 Measured point spread functions for conventional imaging and imaging with a cubic phase. PSFs for conventional system at (a) 113" (2870 mm), (b) 146.5" (3721 mm), and (c) 180" (4572 mm). (d)-(f) PSFs for a system with cubic phase at the same distances for (a)-(c).

3 Compressive imaging

Compressive sampling is a new concept in signal processing and information theory in which one measures a small number of non-adaptive linear combinations of a signal. The number of measurements is usually much smaller than the number of samples that define the signal. From these small number of measurements, the signal is then reconstructed by a non-linear procedure.[4,5]

More precisely, suppose $\mathbf{i}_p \in \mathbb{C}^{N^2}$ is k-sparse in a basis (or a Dictionary) Ψ, so that $\mathbf{i}_p = \Psi\boldsymbol{\alpha}$, with $\| \boldsymbol{\alpha} \|_0 = k \ll N^2$. In the case when $\mathbf{i}_p$ is compressible in Ψ, it can be well approximated by the best k-term representation. Consider a random $n \times N^2$ measurement matrix Φ with $n < N^2$ and assume that n measurements, that make up a vector $\mathbf{i}_o$, are made such that

$$\begin{aligned} \mathbf{i}_o &= \Phi\mathbf{i}_p \\ &= \Phi\Psi\boldsymbol{\alpha} \\ &= \Theta\boldsymbol{\alpha}. \end{aligned}$$

According to CS theory, when Θ satisfies the restricted isometry property (RIP),[16] one can reconstruct $\mathbf{i}_p$ via its coefficients $\boldsymbol{\alpha}$ by solving the following ℓ^1 minimization problem:[4,5]

$$\hat{\boldsymbol{\alpha}} = \arg\min_{\boldsymbol{\alpha}} \| \boldsymbol{\alpha} \|_1 \quad \text{subject to} \quad \mathbf{i}_o = \Phi\Psi\boldsymbol{\alpha}. \tag{8}$$

A matrix Θ is said to satisfy the RIP of order k with constants $\delta_K \in (0, 1)$ if

$$(1 - \delta_k) \| \mathbf{v} \|_2^2 \leq \| \Theta\mathbf{v} \|_2^2 \leq (1 + \delta_k) \| \mathbf{v} \|_2^2 \tag{9}$$

for any $\mathbf{v}$ such that $\| \mathbf{v} \|_0 \leq k$.

In the case of noisy observations, the following optimization problem can be solved to obtain an approximate solution

$$\hat{\boldsymbol{\alpha}} = \arg\min_{\boldsymbol{\alpha}} \| \boldsymbol{\alpha} \|_1 \quad \text{subject to} \quad \|\mathbf{i}_o - \Theta\boldsymbol{\alpha}\|_2 \leq \epsilon. \tag{10}$$

where we have assumed that the observations are of the following form

$$\mathbf{i}_o = \Theta\boldsymbol{\alpha} + \boldsymbol{\eta}, \tag{11}$$

with $\|\boldsymbol{\eta}\|^2 = \epsilon^2$.

One popular class of measurement matrices satisfying an RIP is the one consisting of i.i.d. Gaussian entries. It is a well known fact that if Φ is an $n \times N^2$ Gaussian matrix where $n > \mathcal{O}(k \log N^2)$ and Ψ is a sparsifying basis, then Θ satisfies the RIP with high probability. One can also use greedy pursuits and iterative soft or hard thresholding algorithms to recover signals from compressive measurements.

4 Accelerated imaging with extended depth-of-field

Since our objective is to form mmW images with reduced number of samples, we propose the following sampling strategy. Because our sensor is a single-beam system that produces images by scanning in azimuth and elevation, we can reduce the number of samples by randomly undersampling in both azimuth and elevation. Mathematically, this amounts to introducing a mask in Eq. (1),

$$\begin{aligned} \mathbf{i}_M &= \mathbf{M}\mathbf{i} \\ &= \mathbf{M}\mathbf{H}\mathbf{o}_g, \end{aligned} \tag{12}$$

where $\mathbf{i}_M$ is an $N^2 \times 1$ lexicographically ordered column vector of observations with missing information. Here, $\mathbf{M}$ is a degradation operator that removes p samples from the signal. We construct the $N^2 \times N^2$ matrix $\mathbf{M}$ by replacing p elements in the diagonal of the $N^2 \times N^2$ identity matrix with zeros. The locations of the zeros determines which image samples are discarded.

To account for the Wiener filter in Eq. (5) used to process the intermediate image produced by the cubic phase element, we write the observation model as

$$\begin{aligned} \mathbf{i}_o &= \mathbf{W}\mathbf{i}_M \\ &= \mathbf{W}\mathbf{M}\mathbf{i} \\ &= \mathbf{W}\mathbf{M}\mathbf{H}\mathbf{o}_g. \end{aligned} \tag{13}$$

We use the relation in Eq. (7) to write $\mathbf{H}\mathbf{o}_g$ in terms of the diffraction limited response, $\mathbf{i}_p$,

$$\mathbf{H}\mathbf{o}_g = \mathbf{G}\mathbf{i}_p, \tag{14}$$

where $\mathbf{G}$ is the regularized inverse filter that corresponds to $\mathbf{W}$. With this, and assuming the presence of additive noise η, we rewrite the observation model Eq. (13) as

$$\mathbf{i}_o = \mathbf{W}\mathbf{M}\mathbf{G}\mathbf{i}_p + \boldsymbol{\eta}, \tag{15}$$

where $\boldsymbol{\eta}$ denotes the $N^2 \times 1$ column vector corresponding to noise, η. We assume that $\|\boldsymbol{\eta}\|^2 = \epsilon^2$.

Having observed $\mathbf{i}_o$ and knowing the matrices $\mathbf{W}, \mathbf{M}$ and $\mathbf{G}$, the general problem is to estimate the diffraction limited response, $\mathbf{i}_p$. Assume that $\mathbf{i}_p$ is sparse or compressible in a basis or frame $\boldsymbol{\Psi}$ so that $\mathbf{i}_p = \boldsymbol{\Psi}\boldsymbol{\alpha}$ with $\|\boldsymbol{\alpha}\|_0 = K \ll N^2$, where the ℓ_0 sparsity measure $\|.\|_0$ counts the number of nonzero elements in the representation. The observation model Eq. (15) can now be rewritten as

$$\mathbf{i}_o = \mathbf{W}\mathbf{M}\mathbf{G}\boldsymbol{\Psi}\boldsymbol{\alpha} + \boldsymbol{\eta}. \tag{16}$$

This is a classic inverse problem whose solution can be obtained by solving the following optimization problem

$$\hat{\boldsymbol{\alpha}} = \arg\min_{\boldsymbol{\alpha}} \| \boldsymbol{\alpha} \|_1 \quad \text{subject to} \quad \|\mathbf{i}_o - \mathbf{W}\mathbf{M}\mathbf{G}\boldsymbol{\Psi}\boldsymbol{\alpha}\|_2 \leq \epsilon. \tag{17}$$

One can clearly see the similarity between this problem and the compressed sensing problem discussed in the previous section. Once the representation vector $\boldsymbol{\alpha}$ is estimated, we obtain the final estimate of $\mathbf{i}_p$ as $\hat{\mathbf{i}}_p = \boldsymbol{\Psi}\hat{\boldsymbol{\alpha}}$. Note that the recovery of $\boldsymbol{\alpha}$ from Eq. (16) depends on certain conditions on the sensing matrix $\mathbf{W}\mathbf{M}\mathbf{G}\boldsymbol{\Psi}$ and the sparsity of $\boldsymbol{\alpha}$.[17]

5 Experimental Results

In this section, we demonstrate the performance and applicability of our method on real mmW data. In these experiments, we use an orthogonal wavelet transform (Daubechies 4 wavelet) as a sparsifying transform. There has been a number of approaches suggested for solving optimization

problems such as Eq. (17). In our approach, we employ a highly efficient algorithm that is suitable for large scale applications known as the Gradient Projection for Sparse Reconstruction (GPSR) algorithm.[18]

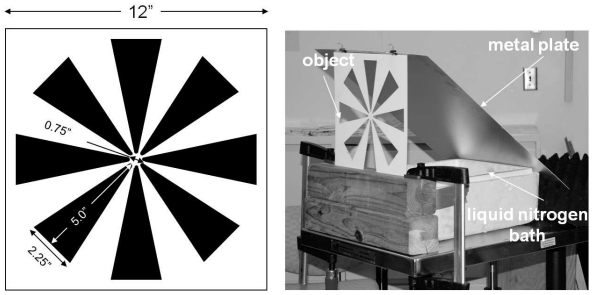

(a) (b)

Fig. 3 (a) Representation of the extended object used to compare conventional and cubic-phase imaging. (b) Schematic of object illumination.

The extended object used in our experiments is represented in Fig. 3(a). Images of an extended object for conventional imaging system at $113”, 146”$ and $180”$ are shown in Fig. 4(a)-(c), respectively. Each image is represented by 41×51 measurements, or pixels. The object size within the image is a function of optical magnification. Note that the conventional imaging system produces images with significant blurring. In contrast, even without signal processing, the images produced with cubic phase element retain more discernable characteristics of the object than the images from the conventional system, as shown in Fig. 4(d)-(f). It can be seen from Fig. 4(g)-(i) that post processing compensates for the effect of the cubic phase element and retains frequency content that is otherwise lost in a conventional system. The wider bandwidth, in addition to the noise suppressing characteristics of the Weiner filter, produce images that appear sharper than those produced by a conventional imaging system. Hence, one can extend the region over which the system generates diffraction limited images. In fact, in,[3] it was shown that the DoF of a conventional 94-GHz imaging system can be extended from 17.4” to more than 68”.

In our first experiment, we used only 50% of the measured data. The samples were discarded according to a random undersampling pattern shown in Fig. 5. Figs. 6(a)-(c) show the sparsely sampled cubic phase data. The reconstructed images obtained by solving problem (17) are shown in Fig. 6(d)-(f). The reconstructions of the extended object are comparable to the processed images from a system with cubic phase. This can be seen by comparing Fig. 4(g)-(i) with Fig. 6(d)-(f). One of the obvious reasons for this is that, although we have reduced the number of measurements by half, a substantial number of them are nonzero. But this will be true in any arbitrary scene and does not detract from our approach.

Nonetheless, to pursue this further, we considered other values of undersampling and their impact on reconstruction. Fig. 7 is a collection of representative recovered images at the three object

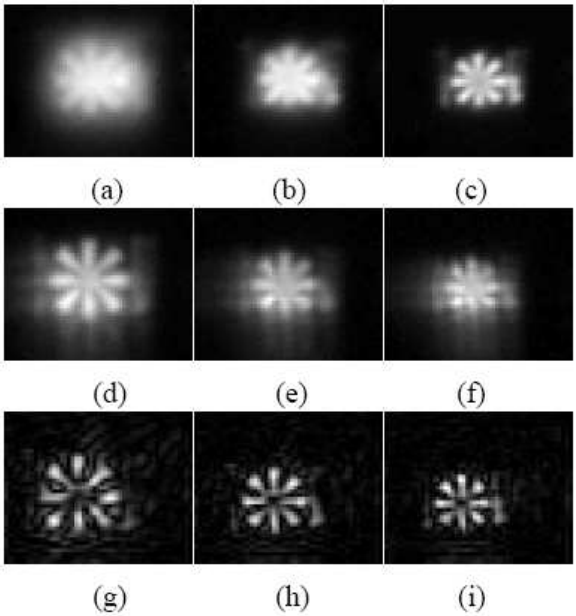

Fig. 4 Images from a conventional imaging system at (a) 113", (b) 146" and (c) 180". (d)-(f) Images from a system with cubic phase at the same object distances as for (a)-(c). (g)-(f) Processed images from a system with cubic phase at the same object distances as for (a)-(c).

Fig. 5 A random undersampling pattern.

distances of interest for measurements between 10% and 40% in increments of 10%. Note that even with only 30% and 40% of the original measurements, our reconstruction is able to recover recognizable characteristics of the original images.

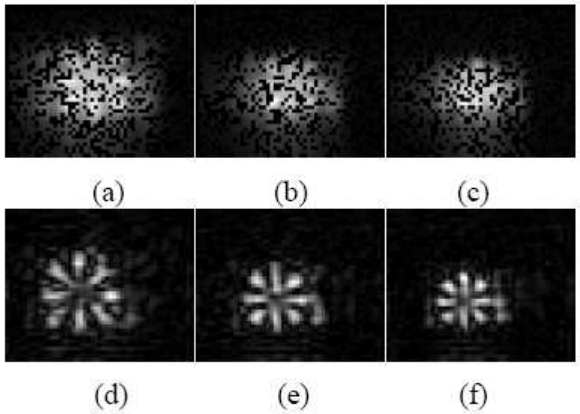

Fig. 6 50% Sparse sampled data from a modified imaging system at (a) 113", (b) 146", and (c) 180". (d)-(f) Diffraction limited images recovered by solving (17) at the same object distances as for (a)-(c).

To quantify the impact of undersampling, we calculated the relative error in images recovered from sparsely sampled data. We define the relative error e_R as

$$e_R = \frac{\|\tilde{\mathbf{x}} - \hat{\mathbf{x}}\|_2}{\|\tilde{\mathbf{x}}\|_2}, \tag{18}$$

where $\tilde{\mathbf{x}}$ corresponds to post processed image with full measurements and $\hat{\mathbf{x}}$ is the estimated image from sparsely sampled data.

For a given undersampling percentage q between 10 and 90 , we generated 10 different random undersampling masks consisting of q measurements. To recover the image, we solved the ℓ_1-minimization problem of Eq. (17) for each mask using the GPSR algorithm and computed e_R. Fig. 8 represents the average relative error for the 10 masks as a function of the number of measurements q.

From Fig. 8, we see that the reconstruction quality generally improves as the number of measurements increases. Furthermore, reconstruction curves corresponding to all three distances 113", 146" and 180" follow a similar pattern, which underscores the depth invariance of the system. Note that, for all three distances, as the number of measurements increases from 10% to 50%, the relative error decreases from about 60% to 25%. This behavior is reflected qualitatively in Fig. 7. After the number of measurements increases beyond 50% the relative error decreases less rapidly. With 90% of the measurements, the relative error is approximately 15%. Taken together, Figs. 6 through 8 indicate the potential to extend depth-of-field using sparsely sampled measurements in a cubic phase system. This is an important capability if one wishes to screen individuals rapidly as they move through a corridor instead of a portal.

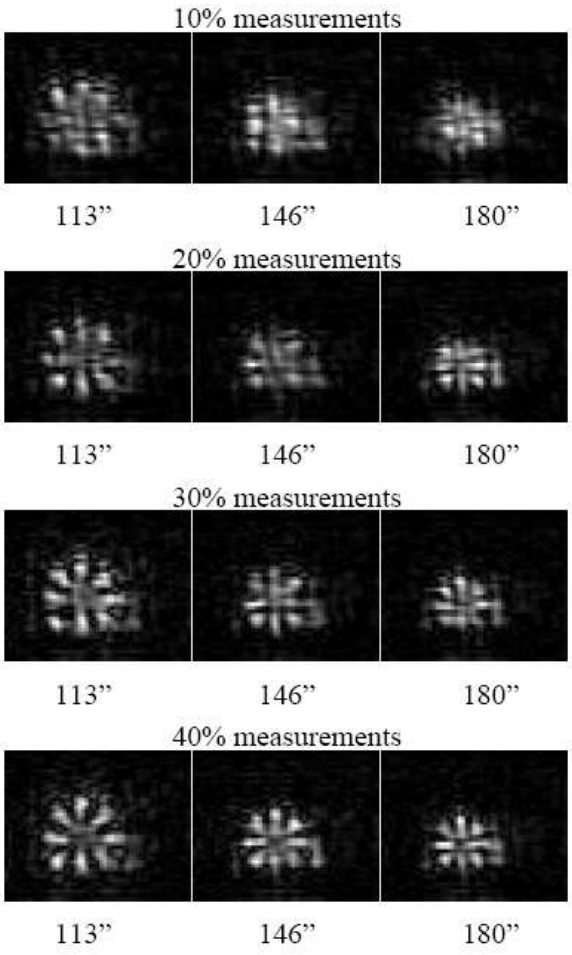

Fig. 7 Diffraction limited images recovered by solving (17) at different object distances from various number of measurements.

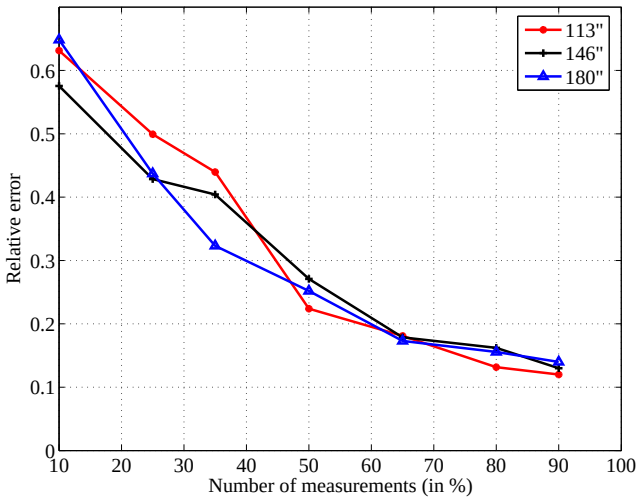

Fig. 8 Relative error vs. number of measurement curves.

6 Discussion and Conclusion

We have utilized a computational imaging technique along with a nonlinear reconstruction method and demonstrated that extended depth-of-field is possible for passive millimeter wave imaging even when the cubic phase data is sparsely sampled. Because millimeter wave systems image temperature contrasts, a careful analysis of noise and contrast in such systems in necessary to assess the true impact of inserting a cubic phase element in the pupil plane of the system and sparsely sampling the data. We are considering a more extensive study using realistic scenes and objects to determine the level of undersampling that one can apply to a general case of mmW imaging, for example, for concealed weapon detection. Our future plan includes the analysis of the artifacts introduced by the cubic phase element and random undersampling in terms of the point spread function as was done in.[19]

Acknowledgments

The authors would like to thank Charles Dietlein of ARL for fruitful observations and comments on our work and to Prof. Rama Chellappa of the University of Maryland for engaging discussions about the project. This work was partially supported by a MURI from the Army Research Office under the Grant W911NF-09-1-0383.

References

1. R. Appleby and R. N. Anderton, "Millimeter-wave and submillimeter-wave imaging for security and surveillance," *Proceedings of the IEEE*, vol. 95, no. 8, pp. 1683 –1690, Aug. 2007.
2. L. Yujiri, M. Shoucri, and P. Moffa, "Passive millimeter wave imaging," *IEEE Microwave Magazine*, vol. 4, no. 3, pp. 39 – 50, sept. 2003.
3. J. Mait, D. Wikner, M. Mirotznik, J. van der Gracht, G. Behrmann, B. Good, and S. Mathews, "94-GHz imager with extended depth of field," *IEEE Transactions on Antennas and Propagation*, vol. 57, no. 6, pp. 1713 –1719, june 2009.
4. D. Donoho, "Compressed sensing," *IEEE Transactions on Information Theory*, vol. 52, no. 4, pp. 1289–1306, Apr. 2006.
5. E. Candes, J. Romberg, and T. Tao, "Robust uncertainty principles: exact signal reconstruction from highly incomplete frequency information," *IEEE Transactions on Information Theory*, vol. 52, no. 2, pp. 489–509, Feb. 2006.
6. S. D. Babacan, M. Luessi, L. Spinoulas, and A. K. Katsaggelos, "Compressive passive millimeter-wave imaging," in *IEEE ICIP*, 2011.
7. N. Gopalsami, T. W. Elmer, S. Liao, R. Ahern, A. Heifetz, A. C. Raptis, M. Luessi, S. D. Babacan, and A. K. Katsaggelos, "Compressive sampling in passive millimeter-wave imaging," in *Proc. SPIE*, vol. 8022, 2011.
8. C. F. Cull, D. A. Wikner, J. N. Mait, M. Mattheiss, and D. J. Brady, "Millimeter-wave compressive holography," *Appl. Opt.*, vol. 49, no. 19, pp. E67–E82, Jul 2010.
9. C. A. Fernandez, D. Brady, J. N. Mait, and D. A. Wikner, "Sparse fourier sampling in millimeter-wave compressive holography," in *Digital Holography and Three-Dimensional Imaging*, 2010, p. JMA14.

10. W. L. Chan, K. Charan, D. Takhar, K. F. Kelly, R. G. Baraniuk, and D. M. Mittleman, "A single-pixel terahertz imaging system based on compressed sensing," *Appl. Phys. Lett.*, vol. 93, no. 12, pp. 121 105–3, 2008.
11. I. Noor, O. Furxhi, and E. L. Jacobs, "Compressive sensing for a sub-millimeter wave single pixel imager," in *Proc. SPIE*, vol. 8022, 2011.
12. J. W. Goodman, *Introduction to Fourier optics*. Englewood, CO: Roberts and Company, 2005.
13. W. T. Cathey and E. R. Dowski, "New paradigm for imaging systems," *Appl. Opt.*, vol. 41, no. 29, pp. 6080–6092, Oct. 2002.
14. J. Edward R. Dowski and W. T. Cathey, "Extended depth of field through wave-front coding," *Appl. Opt.*, vol. 34, no. 11, pp. 1859–1866, Apr. 1995.
15. S. Bradburn, W. T. Cathey, and E. R. Dowski, "Realizations of focus invariance in optical–digital systems with wave-front coding," *Appl. Opt.*, vol. 36, no. 35, pp. 9157–9166, Dec. 1997.
16. E. Candes, J. Romberg, and T. Tao, "Stable signal recovery from incomplete and inaccurate measurements," *Communications on Pure and Applied Mathematics*, vol. 59, no. 8, pp. 1207–1223, August 2006.
17. M. Elad, *Sparse and Redundant Representations: From theory to applications in Signal and Image processing*. Springer, 2010.
18. M. Figueiredo, R. Nowak, and S. Wright, "Gradient projection for sparse reconstruction: Application to compressed sensing and other inverse problems," *IEEE Journal of Selected Topics in Signal Processing*, vol. 1, no. 4, pp. 586 –597, dec. 2007.
19. V. M. Patel, G. R. Easley, D. M. Healy, and R. Chellappa, "Compressed synthetic aperture radar," *IEEE Journal of Selected Topics in Signal Processing*, vol. 4, no. 2, pp. 244 –254, april 2010.

Vishal M. Patel is a member of the research faculty at the University of Maryland Institute for Advanced Computer Studies (UMIACS). He received the B.S. degrees in Electrical Engineering and Applied Mathematics (with honors) and the M.S. degree in Applied Mathematics from North Carolina State University, Raleigh, NC, in 2004 and 2005, respectively. He received his Ph.D. from the University of Maryland, College Park, MD, in Electrical Engineering in 2010. He was an ORAU postdoctoral fellow with the U.S. Army Research Laboratory in 2010.

His research interests are in signal processing, computer vision and patter analysis with applications to radar imaging and biometrics. His published works include compressed sensing, sparse representation, face recognition, iris recognition, synthetic aperture radar imaging and image restoration.

He is a member of Eta Kappa Nu, Pi Mu Epsilon and Phi Beta Kappa.

Joseph N. Mait received his BSEE from the University of Virginia in 1979 and received his graduate degrees from the Georgia Institute of Technology; his MSEE in 1980 and Ph.D. in 1985.

Since 1989 Dr. Mait has been with the U.S. Army Research Laboratory (formerly Harry Diamond Laboratories), where he is presently a senior technical (ST) researcher. Early in his career Dr. Mait was an assistant professor of Electrical Engineering at the University of Virginia. He was also an adjunct associate professor at the University of Maryland, Col-

lege Park, and an adjunct professor at Duke University. He has held visiting positions at the Lehrstuhl für Angewandte Optik, Universität Erlangen-Nürnberg, Germany and the Center for Technology and National Security Policy at the National Defense University in Washington DC.

Dr. Mait's research interests include sensors and the application of optics, photonics, and electromagnetics to sensing and sensor signal processing. Particular research areas include diffractive optic design and computational imaging. He also had an unexpected sojourn into autonomous systems, where for six years he led ARLs program on micro-autonomous systems and technology.

He is currently Editor-in-Chief of Applied Optics. He is a Fellow of SPIE and OSA, and a senior member of IEEE. He is also a member of Sigma Xi, Tau Beta Pi, and Eta Kappa Nu, and is a Raven from the University of Virginia.

List of Figure Captions:

1. Figure 1 Cubic phase element. (a) Side view of the cubic phase element mounted the antenna. (b) Front view. (c) Detail of fabricated cubic phase element.

2. Figure 2 Measured point spread functions for conventional imaging and imaging with a cubic phase. PSFs for conventional system at (a) 113" (2870 mm), (b) 146.5" (3721 mm), and (c) 180" (4572 mm). (d)-(f) PSFs for a system with cubic phase at the same distances for (a)-(c).

3. Figure 3 (a) Representation of the extended object used to compare conventional and cubic-phase imaging. (b) Schematic of object illumination.

4. Figure 4 Images from a conventional imaging system at (a) 113", (b) 146" and (c) 180". (d)-(f) Images from a system with cubic phase at the same object distances as for (a)-(c). (g)-(f) Processed images from a system with cubic phase at the same object distances as for (a)-(c).

5. Figure 5 A random undersampling pattern.

6. Figure 6 50% Sparse sampled data from a modified imaging system at (a) 113", (b) 146", and (c) 180". (d)-(f) Diffraction limited images recovered by solving (17) at the same object distances as for (a)-(c).

7. Figure 7 Diffraction limited images recovered by solving (17) at different object distances from various number of measurements.

8. Figure 8 Relative error vs. number of measurement curves.